Studies of CO2 Hydrogenation over Cobalt/Ceria Catalysts with In-situ Characterization: The Effect of Cobalt Loading and Metal-Support Interactions on the Catalytic Activity

Complete List of Authors:	Deng, Kaixi; Stony Brook University, Chemistry Lin, Lili; Brookhaven National Laboratory, Chemistry Rui, Ning; Brookhaven National Laboratory, Department of Chemistry Vovchok, Dimitriy; Brookhaven National Laboratory, Chemistry Department Zhang, Feng; SUNY Stony Brook, Materials Science & Enginerring Zhang, Shuhao; Stony Brook University, Materials Science and Chemical Engineering Senanayake, Sanjaya; Brookhaven National Laboratory, Chemistry KIM, TAE JIN; Stony Brook University, Materials Science and Chemical Engineering Rodriguez, Jose; Brookhaven National Laboratory, Chemistry Department

Studies of CO$_2$ Hydrogenation over Cobalt/Ceria Catalysts with *in situ* Characterization: The Effect of Cobalt Loading and Metal-Support Interactions on the Catalytic Activity

Kaixi Deng[1], Lili Lin[2], Ning Rui[2], Dimitriy Vovchok[2], Feng Zhang[3], Shuhao Zhang[3], Sanjaya Senanayake[2], Taejin Kim[3], Jose A. Rodriguez[1,2]

1. Department of Chemistry, Stony Brook University, Stony Brook, NY 11794, USA
2. Chemistry Division, Brookhaven National Laboratory, Upton, NY 11973, USA
3. Materials Science and Chemical Engineering Department, Stony Brook University, Stony Brook, NY 11794, USA

Abstract:

The catalytic activities of cobalt/ceria catalysts (Co loadings of 1, 2 and 4wt%) for CO$_2$ hydrogenation at 250°C were measured. When catalyzed by samples with the same mass of cobalt, the CO$_2$ conversion showed a trend where 4wt% ≈ 2wt% > 1wt%. XRD results combined with XANES data of pristine and reduced samples showed that the size of the cobalt particles was proportional to the admetal loading. Moreover, XANES data of reduced catalysts indicated that samples with higher loading have a higher percentage of metallic cobalt while a significant part of cobalt in the 1wt% Co/CeO$_2$ sample remains as CoO$_x$ after reduction By analyzing EXAFS data, it was found that the Co-O bond in the 1wt% and 2wt% Co/CeO$_2$ was about 0.16 Å shorter than that of standard CoO, which explains its stability during the reduction process. The positive charge on the cobalt atoms substantially affected the surface chemistry of the CO$_2$ hydrogenation process. *In situ* DRIFTS experiments under reaction conditions showed that the Ce^{3+} site density on the surface of the 1wt% Co/CeO$_2$ catalyst was much lower than that of the other two samples. In addition, formates were found to be spectators in the 1wt% sample while they could be further hydrogenated in the 2wt% and 4wt% Co/CeO$_2$ surfaces. Based on these results, we propose that the strong perturbations on the structural and electronic properties, which cause positively charged cobalt atoms in the cobalt-ceria interface, make the highly dispersed cobalt on ceria less active for activating hydrogen leading to a lower CO$_2$ hydrogenation efficiency in the case of 1wt% Co/CeO$_2$.

Introduction:

The CO$_2$ hydrogenation reaction is considered as a promising solution to the increased CO$_2$ level in the atmosphere. With different catalysts, CO$_2$ can be hydrogenated into CO, CH$_4$[1], CH$_3$OH[2] and ≥ C2 chemicals [3] including ethanol[4], olefins[5] and gasoline fuel[6]. A common type of catalysts for CO$_2$ hydrogenation comprises of a metal and an oxide. [7-9] During the reaction, H$_2$ usually dissociates on the metals [10] while the oxide helps to activate CO$_2$[8]. Many metals are found to be active in CO$_2$ hydrogenation including primarily Pt, Pd, Ru, Rh, Cu, Ni and Co. [7] Among them, Cu, Ni and Co are abundant metals which have higher potential for applications considering their much lower cost. Each of these three metals has its special properties in catalyzing CO$_2$ hydrogenation reactions: Cu based catalysts are primarily studied for methanol production at high pressure and the reverse water gas shift at low pressure [8]; Ni based catalysts are known for their CO$_2$ methanation ability [11]; and Co based catalysts are primarily aimed at the Fischer–Tropsch process[12, 13]. Even though only a few cobalt based catalysts have been studied for CO$_2$ hydrogenation, they have been reported to produce short chain

alkanes [14]. Different from Cu and Ni, CO_2 is found to dissociate on the cobalt surface even without the help of hydrogen as cobalt has a higher tendency to bond with oxygen[15, 16]. Because of this, most studies about cobalt-based catalysts for CO_2 hydrogenation used inert materials as supports. While studies using cobalt supported by an active oxide for catalyzing CO_2 hydrogenation are uncommon, it has been reported that an active oxide support can promote CO_2 conversion. Recently, Díez-Ramírez et al reported that a Co/CeO_2 catalyst shows superior CO_2 hydrogenation activity compared to Co supported on ZrO_2, Gd_2O_3, and ZnO due to its enhanced reducibility [17]. In comparison with other oxides, the cation-O bonds in CeO_2 are easier to break and re-form making this system more efficient for activating CO_2 molecules.[18,19] In addition, previous works also suggest that oxygen atoms from CeO_2 have a higher tendency to be transferred or shared with supported metals.[17] In separate studies, it has been indicated that supported metals forming small clusters tend to strongly interact with the oxide support making their catalytic activity deviate from that of big metal particles[20, 21]. This is a highly intriguing subject as is worth to invetigate its existence in Co/CeO_2 systems since it can provide a tool or approach for the rational design of better catalysts.

In this study, the combination of cobalt and ceria is selected for three main reasons: First, the pair could have a strong metal-support interaction as cobalt tends to strongly bond with oxygen while ceria is an active oxygen provider; Second, the cobalt/ceria combination has been reported to have good activity for CO_2 hydrogenation[17]; And third, there is no prior study focussed on examining metal-support interactions between cobalt and ceria and their impact on the CO_2 hydrogenation activity. In this study, cobalt loads of 1, 2 and 4wt% were dispersed on a ceria support with the aim of getting different metal particle sizes[22,23]. The CO_2 hydrogenation efficiency was found to follow the sequence: 4wt% > 2wt% > 1wt%. The effects of strong metal-support interactions led to the disappearance of the Fischer–Tropsch ability of cobalt. In addition to *in-situ* X-ray absorption spectroscopy, surface sensitive characterization techniques such as near ambient pressure X-ray photoelectron spectroscopy (NAP-XPS) and *in situ* diffuse reflectance infrared Fourier transform spectroscopy (DRIFTS) were employed to study the chemial state of the catalysts and the associated surface chemistry for CO_2 hydrogenation.

Experimental section:
Catalyst preparation:

Details of the synthesis method used in this study for the preparation of the cobalt-ceria catalysts has been published elsewhere.[24] In brief, the ceria (HSA5, Rhodia) supported cobalt catalysts (Co/CeO_2) were prepared by incipient wetness impregnation of an aqueous solution with varying concentrations of cobalt (II) nitrate hexahydrate $Co(NO_3)_2 \cdot 6H_2O$ onto the CeO_2 support. After impregnation, the samples were dried and subsequently calcined at 400 °C for 6 hours in air.

Catalytic activity measurements

The catalytic performance of catalysts was evaluated in a continuous-flow, fixed-bed microreactor at about 1 atm pressure. Samples containing 0.08 mg of cobalt were mounted in a quartz tube reactor with quartz wool. For example, 8 mg of 1wt%Co/CeO_2, 4 mg of 2wt%Co/CeO_2 and 2 mg of 4wt%Co/CeO_2 were used in their activity test to make the total cobalt mass the same for each measurement. To obtain a very good performance, the as-prepared catalysts were initailly reduced in hydrogen. Each catalyst was pretreated in 10 sccm H_2 for 40 min at 450 °C with a ramping rate of 10 °C/min. After cooling down at a rate of about 5 °C/min to 250 °C in H_2, 25 sccm H_2, 5 sccm CO_2 and 5 sccm Ar were introduced into the reactor. The concentrations of gas evolved were analyzed with a gas chromatography instrument (Agilent 7890A) equipped with both flame ionization and thermal

conductivity detectors. The reactivity was monitored in a total 8-hour experiment. The Ar in the gas flow was used as the internal standard.

$$CO_2 \text{ conversion } \% = \frac{F(CH_4)_{outlet} + F(CO)_{outlet}}{F(CO_2)_{inlet}} \%$$

$$CH_4 \text{ selectivity } \% = \frac{F(CH_4)_{outlet}}{F(CH_4)_{outlet} + F(CO)_{outlet}} \%$$

F is the amount of certain reactants or products in the units of mol/s.

Catalyst characterization

BET Surface Area

The specific surface area of Co/CeO_2 catalysts were calculated from N_2 adsorption/ desorption isotherms using the Brunauer-Emmett-Teller (BET) theory. The Micromeritics ASAP 2010 device was used at the liquid N_2 temperature of -196 °C for analysis. Before the analysis, 0.1 g of catalyst was pretreated in vacuum at 300 °C for 4 hours to remove water and impurities.

Inductively Coupled Plasma Atomic Emission Spectrometry (ICP-OES)

The Co element content in the series of Co/CeO_2 catalysts was determined by the ICP-OES technique. The ICP-OES experiment was carried out with an iCAP 6000 Series ICP-OES spectrometer (Thermo Fisher Scientific) equipped with an ASX-260 Autosampler (CETAC). The samples were dissolved in nitric acid before testing. A cobalt standard (1000 mg/L Co in 2% nitric acid, Sigma-Aldrich) was used as the reference.

X-ray Diffraction (XRD)

The X-ray diffraction patterns of the Co/CeO_2 samples were collected at the Advanced Photon Source (APS) 17-BM beamline with an X-ray wavelength of 0.24100 Å. The samples were loaded in a Clausen cell flow reactor with a quartz capillary tube (1.1 mm outside diameter (OD), 0.9 mm internal diameter (ID)). The CeO_2 phase in the XRD data was analyzed using the Rietveld method as implemented in the GSAS II software [25, 26].

X-ray Absorption Spectroscopy (XAS)

The X-ray absorption fine structure (XAFS) spectra of the catalysts were collected at the 8-ID Inner-Shell Spectroscopy (ISS) beamline of the National Synchrotron Light Source II (NSLS-II), Brookhaven National Laboratory (BNL), which is a high flux (10^{14} ph/sec at 10 keV) beamline. In the tests, powder samples were loaded into quartz tubes with 1.0 mm OD and 0.9 mm ID. The Co K-edge XAS spectra were collected in the fluorescence-yield (FLY) detection mode and calibrated with a Co foil as a standard. The spectra were collected at 250 °C with samples in H_2 environment after they were reduced at 450 °C for 30 mins in an H_2 flow. The X-ray absorption near edge structure (XANES) and EXAFS data were processed using the Athena graphical interface [27] based on the IFEFFIT program suite[28]. The E_0 was determined using the "Fraction of edge step" algorithm in IFEFFIT.

Near Ambient Pressure X-ray Photoelectron Spectroscopy (NAP-XPS)

The ambient pressure X-ray photoelectron spectroscopy (AP-XPS) spectra were collected using a SPECS AP-XPS chamber equipped with a PHOIBOS 150 EP MCD-9 analyzer with an energy

resolution of 0.4 eV at the Chemistry Department of BNL. The standard Ce $3d_{3/2}$ binding energy (916.9eV) of Ce(IV)O$_2$ was used for energy calibration. Typically, the fresh sample was pre-treated in the NAP-XPS chamber by a 20 mTorr H$_2$ at 527 °C for 1 h. After pre-treatment, the XPS spectra of the pre-treated samples were collected under UHV at 25 °C. And then a 30 mTorr CO$_2$/H$_2$ (1:5 v/v) mixture was subsequently introduced to the chamber before the reaction temperature was raised to 250 °C. The spectra at the Ce 3d, O 1s, C 1s, and Co 2p regions were collected. Ce 3d regions were energy-corrected according to the U''' component of the Ce 3d core line with a characteristic binding energy of 916.9 eV. The deconvolution fitting of the Ce 3d region was carried out using the CasaXPS code. "E Tougaard" type functions were used as background and the asymmetric line shape for the Ce 3d u and v features[29-31] were fitted with an asymmetric modified Gaussian line-shape while the other peaks were fitted with a Gaussian/Lorentzian convolution[32].

Diffuse Reflectance Infrared Fourier Transform Spectroscopy (DRIFTS)

In situ DRIFTS spectra were collected using an FTIR spectrometer (Bruker Vertex 70) equipped with a Harrick cell and MCT detector at the Chemistry Department of BNL. The catalyst was reduced in H$_2$ 10 sccm at 450 °C for 1 h and then it was cooled down to 250 °C in the H$_2$ flow. Backgrounds were then collected at 250 °C in H$_2$ on corresponding samples before introduction of reaction gases. The compositions of reactants were: 1 sccm CO$_2$, 1 sccm He, and 5 sccm H$_2$ at 250 °C, 1 atm.

For *in situ* DRIFTS data collected in the flow system, regular in situ DRIFT experiments with continuous gas flow, each data point was collected using 128 scans and took 1 min acquisition time. For the data collected at the close system, each data point involved 64 scans and took 0.5 min. The following procedure was applied for the closed system experiments: First, the DRIFTS cell was filled with H$_2$; Second, CO$_2$ was added to the cell to generate a CO$_2$/H$_2$ reaction mixture; And third, the valves were closed as in a batch reactor, the temperature was adjusted to the desired value, and IR was used to monitor the CO$_2$ hydrogenation. The data were processed with the Kubelka-Monk (K-M) equation to deduct the background. The evolution of different species during the reaction was monitored according to the intensity of following positions: CH$_4$ gas phase (3016 cm^{-1}), adsorbed CO (1920-1990 cm^{-1}) and formate (2709-2710 cm^{-1})

Results and discussion:

Table 1. The ICP-OES and BET surface area of catalysts as synthesized.

Sample	Co wt % by ICP-OES	Co wt% Difference (Calculated/ICP-OES)	Specific surface area (m$_2$/g)
CeO$_2$			235
1wt%Co/CeO$_2$	1.0	1.00	182
2wt%Co/CeO$_2$	2.1	0.95	191
4wt%Co/CeO$_2$	3.8	1.05	180

The cobalt loadings and BET surface area of Co/CeO$_2$ catalysts were measured and the results are listed in **Table 1**. The ICP-OES results indicate that the actual cobalt loadings are close to their preparation values and all the tested Co/CeO$_2$ catalysts have similar BET surface area.
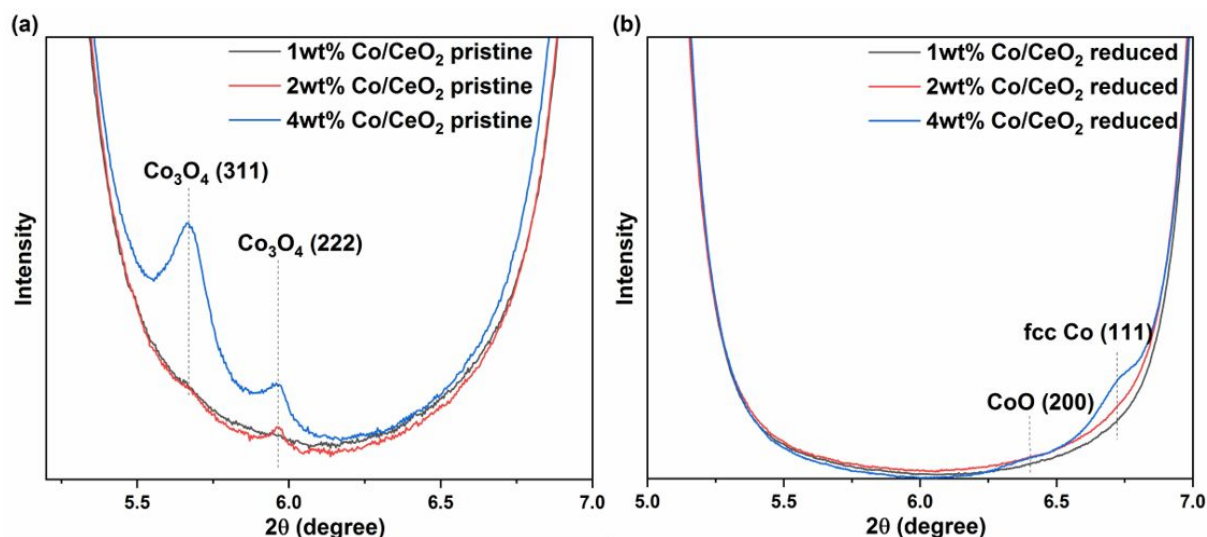
Figure 1. Synchrotron XRD results in the region with signals of cobalt containing species of 1wt%Co/CeO$_2$, 2wt%Co/CeO$_2$ and 4wt%Co/CeO$_2$ in their (**a**) pristine states and (**b**) after reduction at 450 °C in H$_2$.

Synchrotron XRD measurements were carried out with pristine and reduced samples, and the results are shown in **Figure 1 and S1.A (Supporting Information)**. From the full data in **Figure S1.A**, it is clear that the ceria phase is very similar for samples with different cobalt loadings. According to our Rietveld refinement[26] results (**Figure S1.B** and **Table S1**), the crystal size for the CeO$_2$ were 12 nm and 14 nm for pristine and reduced catalysts, respectively. The results confirm that the CeO$_2$ structures

were stable since the ceria was only slightly sintered after reduction at 450℃. **Figure 1** highlights the

region with the most intensive signal from the cobalt-based phases. Peaks corresponding to Co$_3$O$_4$ were observed in the pristine 2 and 4wt% Co/CeO$_2$ samples while no cobalt-based peaks were observed from the 1wt% sample (**1a**), which indicates that the cobalt species in the 1wt%Co/CeO$_2$ is well dispersed or probably amorphous. After reduction, peak features from metallic cobalt and a CoO phase were observed only in the 4wt%Co/CeO$_2$ (**1b**), indicating that cobalt oxides were reduced and formed metallic cobalt particles with a dimension of not less than 2 - 2.5 nm (the limit of conventional X-ray powder diffraction detection [33]). The disappeared cobalt-based XRD peaks in the 2wt% Co/CeO$_2$ indicates that the Co$_3$O$_4$ particles in its pristine sample have been converted to some highly dispersed or amorphous cobalt species after reduction. The XRD patterns of reduced samples clearly indicate that the 4wt%Co/CeO$_2$ has the largest dimension of metallic cobalt among the series even though a reliable cobalt particle size cannot be obtained by Rietveld refinement or the Sherrer equation.

Since amorphous or small size (usually less than 2 nm) cobalt/cobalt oxides do not show in XRD patterns, *in situ* XANES measurements (**Figure 2**) were carried out to investigate the valence state of cobalt in the catalysts. The data were analyzed by linear combination fitting (LCF) and the results are shown in **Figure S3.A** (LCF on the flattened μ(E)) and **S3.B** (LCF on the derivative flattened μ(E)). The values of each analysis can be found on **Table S2.A**. It is noticeable that the valence states of cobalt are very different in the pristine and reduced Co/CeO$_2$ samples as shown in **Figure 3.**
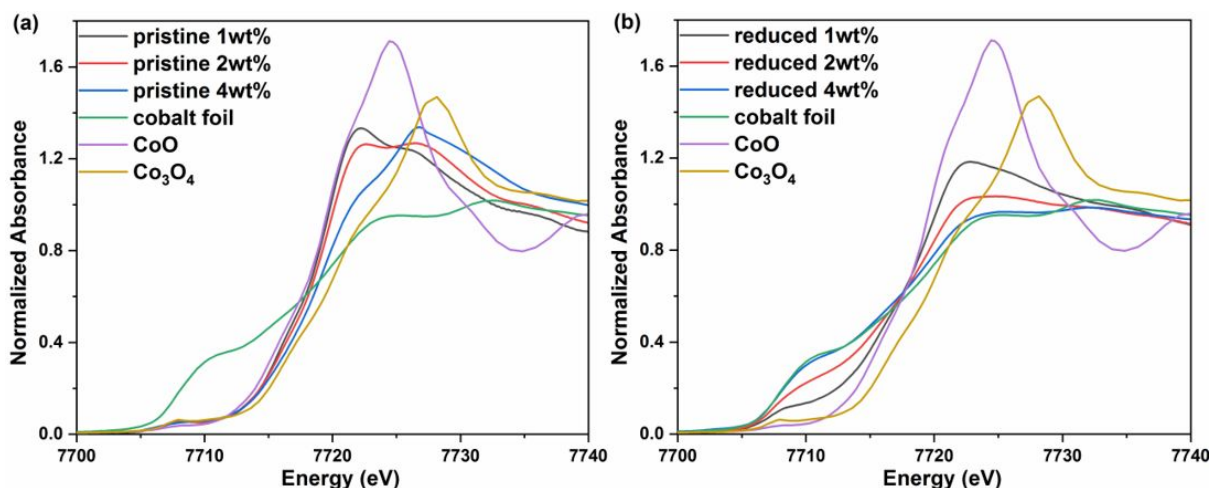
Figure 2. Co *K*-edge XANES spectra of (**a**) pristine and (**b**) reduced samples of cobalt-ceria. Spectra for cobalt foil, CoO and Co_3O_4 are also shown for comparison.
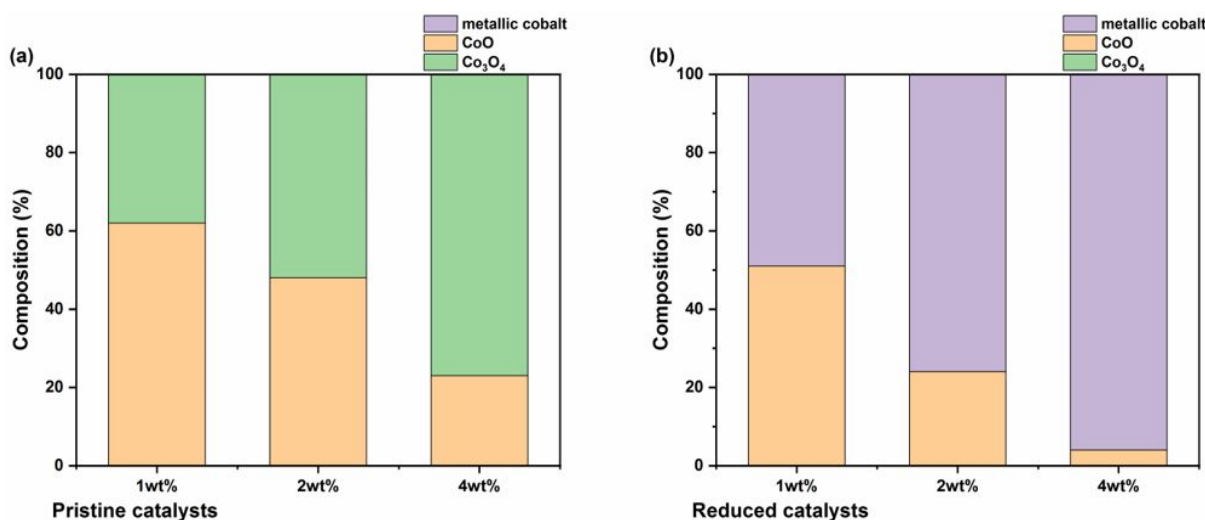

Figure 3. Composition of the three Co/CeO_2 catalysts determined by linear combination fitting of the rough XANES data (**Figure 2**) for the (**a**) pristine and (**b**) reduced states.

Based on the LCF analysis (flattened or derivative $\mu(E)$), it is clear that CoO accounts for a considerable percentage in the 1wt% and 2wt% systems while Co_3O_4 dominates in 4wt%Co/CeO_2. According to the T-p(O_2) phase diagram of Co-O system, the Co_3O_4 is the stable phase for bulk materials at the synthesis conditions of our samples which were calcined at 400 °C in air [34]. This suggests part of the cobalt in our samples has a strong interaction with CeO_2 increasing the stability of CoO. Since a stronger interaction is expected near the cobalt/ceria interface and smaller cobalt particles should have a larger interface fraction, the CoO concentration in pristine samples should be inversely proportional to the cobalt particle size. With these assumptions, the trend of cobalt particle size on the pristine samples can be deduced from the XANES data: 4wt% > 2wt% > 1wt%. As for the reduced samples, the CoO_x near the interface is more difficult to convert into metallic cobalt due to metal-support interaction [35]. In a study on a similar system, a positive charge copper layer has been identified on the Cu/ceria interface after reducing in hydrogen at a temperature as high as 773 K[36]. Therefore, the remaining CoO concentration in the reduced samples should reflect the relative amount of the cobalt

atoms near the cobalt/ceria interface. As **Figure 3b** shows, the relative amount of the CoO for the reduced samples follows the trend 1wt% > 2wt% > 4wt%, which suggests the same trend of cobalt particle size as deduced from the XANES data of the pristine samples. Similar trend is also found when comparing the decrease of CoO percentage during reduction (**Table S2.B**), which follows 1wt% < 2wt% < 4wt%. It is noteworthy that the quality of the LCF for the 1wt% and 2wt% are not good while a much better fitting quality was achieved in the 4wt% Co/CeO$_2$ (**Figure S3.A, S3.B**). The poor fitting quality suggests a large distortion of cobalt structure in the catalysts from the standard bulk materials.
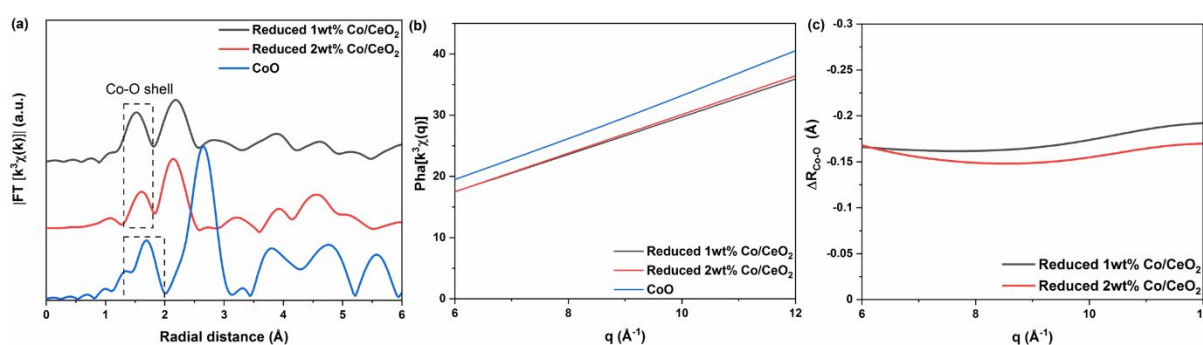

Figure 4. (a)The magnitude of χ(R) (FT [k^3χ(R)]) for 1wt% Co/CeO$_2$, 1wt% Co/CeO$_2$ and CoO (b) the reverse Fourier transform result of χ(R) in the first Co-O shell region (R = 1.3 ~ 1.8 Å for reduced 1wt% Co/CeO2 and reduced 2wt% Co/CeO$_2$, R = 1.3 ~ 2.0 Å for CoO (c) The first shell Co-O bond length difference (evaluated with method detailed in the SI) in compared with standard CoO for reduced 1wt% Co/CeO$_2$, 2wt% Co/CeO$_2$

To get more information about the cobalt structure in our catalysts, their EXAFS data were extracted and compared to the standard CoO and Co$_3$O$_4$ as shown in **Figure S4.A**. Fitting results on the Co-Co shell for the χ(R) of 4wt% Co/CeO$_2$ are shown in **Figure S4.B** and **Table S3.A**. According to a theoretical study on metal half sphere particle of fcc structure, within certain range, there is a relationship between the 1st shell coordination number and the particle size[37]. Using the relationship, the cobalt particle size of the reduced 4wt%Co/CeO$_2$ is determined to be around 2.5 nm with upper limit and lower limit 3.3 nm and 2.0 nm, respectively. As for the 1wt% and 2wt% Co/CeO$_2$, a reliable fitting cannot be achieved probably due to the limited data quality. However, we were still able to evaluate deviation of their Co-O bond length in the first shell from the standard CoO using a method based on Fourier filtering and transferability of phase shifts [38, 39]. And the details about the analysis is in the supporting information. As shown in **Figure 4 c**, **Figure S4.C** and **Table S3.C,** the Co-O bond length in the 1wt% and 2wt% is shorter than that of CoO by about 0.16 Å. This is an important information as it confirms that the cobalt in the reduced catalysts not only do not have a typical CoO crystal structure but the local structure around Co is also quite different. The stronger bonding than that of standard CoO explains their stability under reduction condition. As we will show in the following sections, even though the strong Co-O bonding is detected in both 1wt% and 2wt% Co/CeO$_2$ catalysts, its impact on their catalytic activities is very different.

Catalyst samples with a same cobalt mass (8 mg of 1 wt%Co/CeO$_2$, 4 mg of 2wt%Co/CeO$_2$ and 2 mg of 4wt%Co/CeO$_2$) were used in the activity tests. The tests were carried out at high space velocity conditions (437.5 L/g$_{cobalt}$/min) to eliminate the influence of equilibrium. Under CO$_2$ hydrogenation conditions, CO and CH$_4$ were the only detected products in our GC. As a control, the CeO$_2$ (supporting material) was confirmed to show no activity at the same conditions. As seen in **Figure 5 a, b**, the CO$_2$

conversion shows a trend with 4wt% ≈ 2wt% > 1wt% while CH_4 selectivity of 1wt% is also significantly lower than the other two. As the total mass of cobalt (0.08 mg) is the same for all three samples in the activity tests, the efficiency of converting CO_2 (e.g., consumed CO_2 mole/min/surface area of cobalt) follows the trend 4wt% > 2wt% > 1wt% considering different cobalt surface area resulting from their particle size difference. The results are similar to a study for CO_2 hydrogenation on well-defined cobalt nanoparticles supported on mesoporous silica which concludes that the conversion of CO_2 per surface cobalt atom has the trend 3 nm < 7 nm < 10 nm [40, 41]. The different cobalt particle sizes and oxidation states could also be responsible for the low CH_4 selectivity in 1wt%Co/CeO$_2$ as similar result was reported in Rh-based catalysts[42]. It is clear that the interaction between cobalt and ceria on the interface has a much larger influence on the catalytic activity of 1wt% Co/CeO$_2$. Considering its smaller cobalt particle size, this is understandable since the perturbation on the structure and electronic properties from the cobalt atoms strongly bound to oxygen on the interface is expected to be influential only at a short distance.
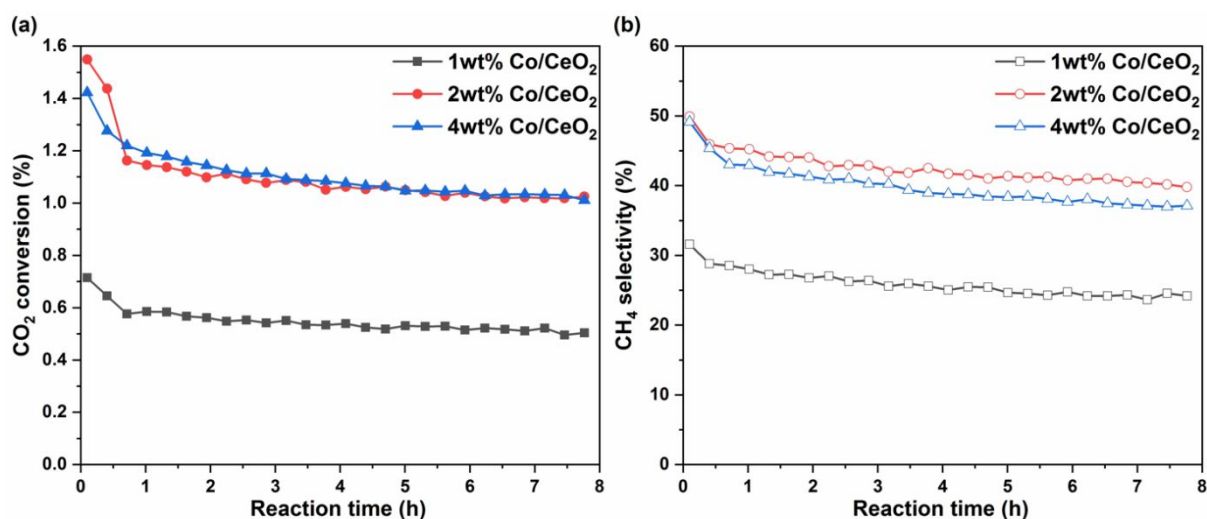

Figure 5. (**a**) CO_2 conversion and (**b**) CH_4 selectivity obtained at fixed space-velocity on 437.5 [L/g$_{cobalt}$/min] for 1wt%Co/CeO$_2$, 2wt%Co/CeO$_2$ and 4wt%Co/CeO$_2$ at 250 °C, 1 atm, H_2/Ar/CO$_2$ (5:1:1 v/v/v). 8 mg of 1wt%Co/CeO$_2$, 4 mg of 2wt%Co/CeO$_2$ and 2 mg of 4wt%Co/CeO$_2$ were used in these activity and selectivity tests.

Since our XRD and XANES measurements are not surface sensitive, NAP-XPS was employed to investigate the inherent difference between Co/CeO$_2$ catalysts of different metal loadings under reduction with pure H_2 and CO_2 hydrogenation conditions. The pristine and reduced samples were examined in UHV conditions at 25 °C and *in situ* characterization was carried out at 250 °C with 25 mTorr H_2 and 5 mTorr CO_2 after the samples were reduced in H_2 at 527 °C for 1h. A higher reduction temperature was applied as the H_2 partial pressure in the NAP-XPS experiments was much lower than that used in the activity measurements and other characterizations. The Ce 3*d* XPS data for the three Co/CeO$_2$ samples are shown at **Figure 6 a, b, c**. The Ce 3d data were analyzed by deconvolution fitting according to literature[43] as shown in **Figure S2** and the percentage of Ce^{3+} peak area at different conditions were summarized in **Table 2**. In the case of the pristine samples, the 1wt% sample has a significantly higher Ce^{3+} concentration than the other two as indicated by the values in **Table 2**, which could be caused by substitution of Ce^{4+} by Co^{2+} on the CeO$_2$ surface[44]. Such substitution has been

reported in other cobalt-based catalysts with low loadings synthesized by incipient-wetness impregnation [23, 45]. The result agrees with our XANES analysis of the pristine 1wt% sample as it infers stronger interaction between cobalt oxides and CeO_2 than for the other two samples. After hydrogen treatment, a noticeable ceria reduction was observed in the 2 and 4wt% samples as their Ce^{3+} percentages increase to 35% from 10% and 12%, respectively. No significant change was observed in 1wt%Co/CeO_2 compared with the pristine sample. It has been reported that the incorporation of cobalt onto ceria based catalysts not only lowers the reduction temperature of ceria surface oxygen but also enables a higher degree of reduction at the temperature range of 400 to 550 °C due to hydrogen spill-over from cobalt to ceria [46, 47]. Similarly, the observed significantly higher ceria reduction degree in 2 and 4wt% catalysts suggests their better hydrogen activation ability in the cobalt species than that of 1wt% Co/CeO_2. At CO_2 hydrogenation reaction conditions, percentage of Ce^{3+} in both 2 and 4wt% samples decreases from 35% to 28% and 26%, respectively, which indicates a re-oxidation of ceria caused by CO_2 dissociation on its surface. In contrast, no significant change in I_{886eV}/I_{889eV} ratio was detected in the same process for the 1wt% sample. **Figure 6 d** shows the Co 2p XPS data of 4%Co/CeO_2 under different conditions. The high noise level is a consequence of the low amount of Co in the sample. However, it is clear that the majority of the cobalt was in a Co^0 state after reduction and in mild reaction conditions. In the case of the 1wt% and 2wt% Co/CeO_2 samples, the Co 2p signals in NAP-XPS were too weak to analyze.
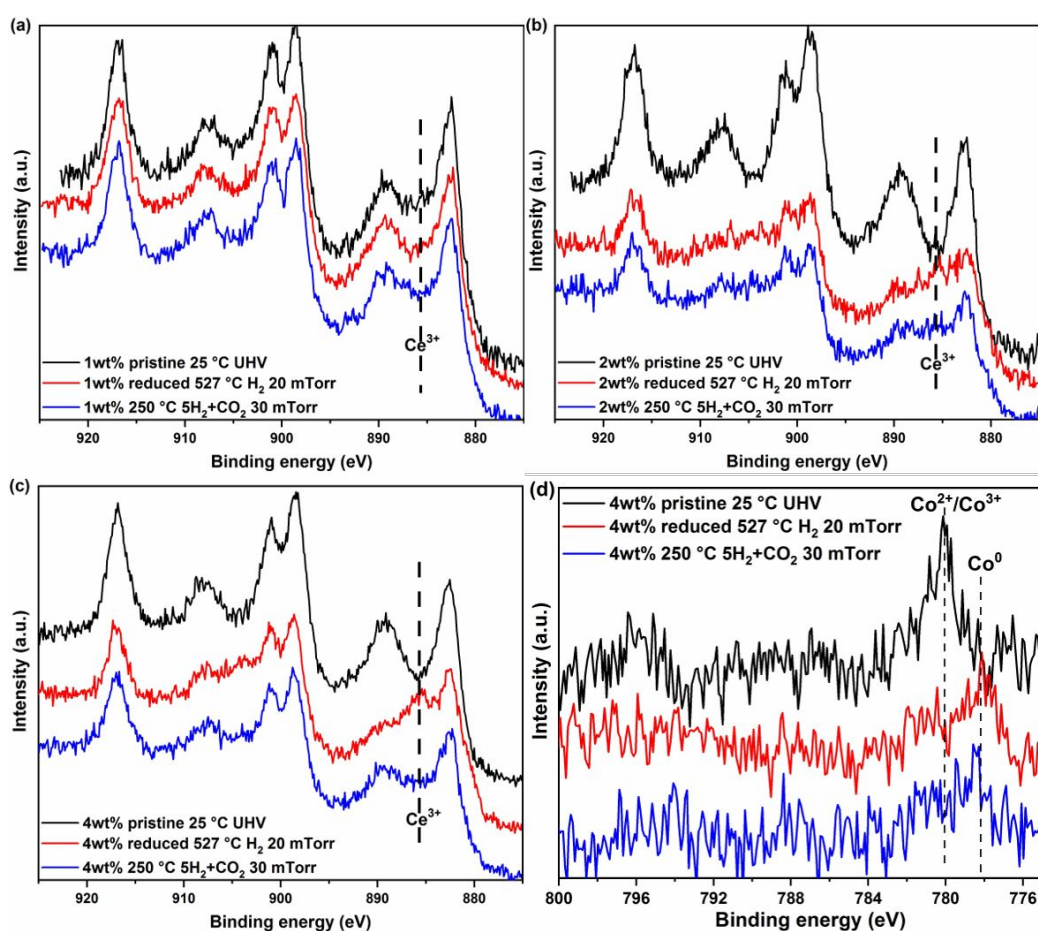

Figure 6. Ce 3d XPS data for (**a**) 1wt%Co/CeO_2, (**b**) 2wt%Co/CeO_2 (**c**) 4wt%Co/CeO_2 and (**d**) Co 2p XPS data of 4wt%Co/CeO_2 at different conditions. The profiles from top to bottom are fresh samples

in UHV at 25 °C (black traces), reduced samples in 20 mTorr H_2 at 527 °C with spectrum recorded in UHV at 25 °C (red traces), and samples at 250 °C with 30 mTorr total pressure of CO_2/H_2 (1:5 v/v) (blue traces).

Table 2. The peak area percentage $S(Ce^{3+})/ S (Ce^{3+} + Ce^{4+})$ evaluated from peak deconvolution fitting on Ce 3d NAP-XPS data.

	Pristine at 25 °C UHV	Reduced at 527 °C H_2 20 mTorr	250 °C 5 H_2 + CO_2 30 mTorr
1wt %Co/CeO$_2$	25 %	23 %	23 %
2wt %Co/CeO$_2$	10 %	35 %	28 %
4wt %Co/CeO$_2$	12 %	35 %	26 %

To get information about adsorbed species on the catalyst surfaces under reaction conditions, *in situ* DRIFTS experiments were carried out at 250 °C and 1 atm total pressure with continuous gas flow over the reduced catalysts. The samples were pre-treated in H_2 at 450 °C for 1 hour and then exposed to a CO_2/H_2 mixture at 250 ºC (was introduced at "0 min" label in the IR figures shown below and in Supporting Information). An analysis of the DRIFTS spectra showed the presence of carbonate and hydrogencarbonate species on the catalyst surfaces.
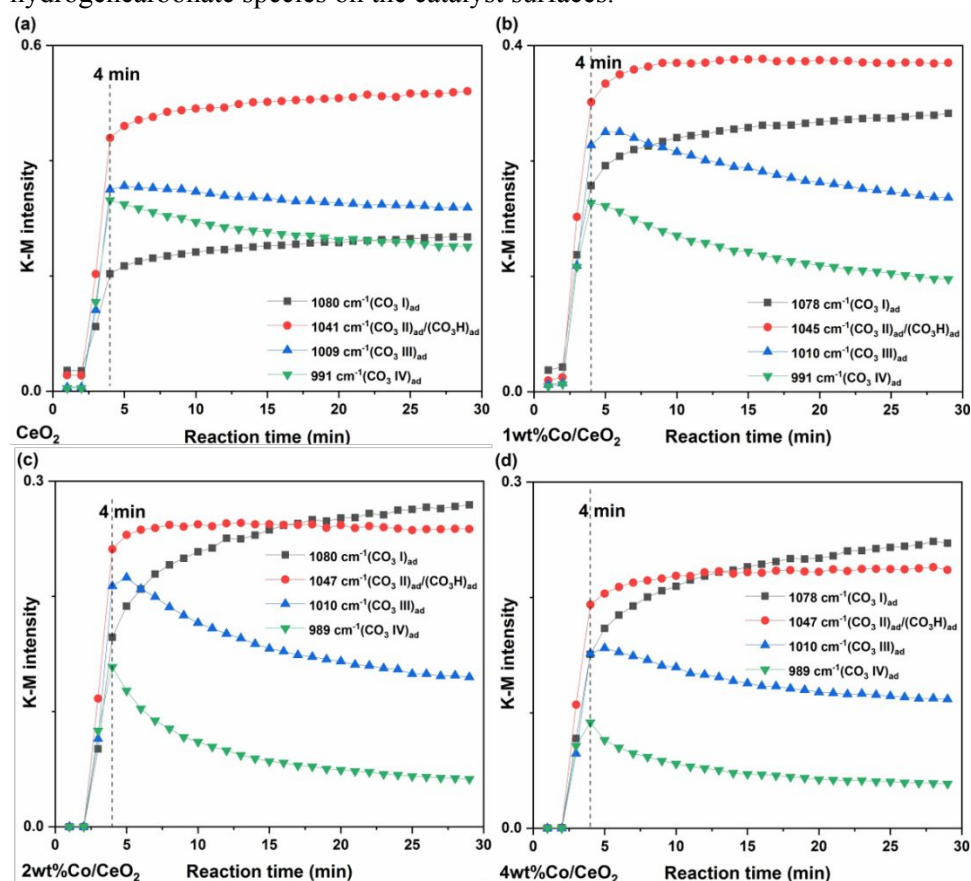

Figure 7. The evolution of carbonate and hydrogencarbonate species on (**a**) CeO$_2$, (**b**) 1wt%Co/CeO$_2$, (**c**) 2wt% Co/CeO$_2$ and (**d**) 4wt% Co/CeO$_2$ in the region of 1200-1700 cm^{-1} collected by *in situ* DRIFTS at 250 ºC and 1 atm. Gases were switched from {5 sccm H_2, 2 sccm He} to {5 sccm H_2, 1 sccm CO_2, 1 sccm He} at the 0 minute time.

Table 3. Peak assignments and notations used in this article

Wavenumber (cm^{-1})	Vibration mode	Assigned species	Ref.
1075 ~ 1085	ν(CO)	Type I carbonate: polydentate carbonate (tridentate in [48]) on Ce^{3+} (CO$_3$ I)$_{ad}$	[48]
1041 ~ 1051	ν(CO)	Type II carbonate: polydentate carbonate (tridentate in [48]) on Ce^{4+} (CO$_3$ II)$_{ad}$ /hydrogencarbonate (CO$_3$H)$_{ad}$	[48-50]
1009 ~ 1015	ν(CO)	Type III carbonate: bidentate carbonate (tridentate in [48]) (CO$_3$ III)$_{ad}$	[48, 50-52]
990 ~ 992	ν(CO)	Type IV carbonate: bidentate carbonate (tridentate in [48]) (CO$_3$ IV)$_{ad}$	[48]
2703	2δ(OCH)	Type I formate: formate I on Ce^{3+} (HCOO I)$_{ad}$	[53-56]
2709 ~ 2710	2δ(OCH)	Type II formate: formate II on Ce^{3+} (HCOO II)$_{ad}$	
2715 ~ 2720	2δ(OCH)	Type III formate: formate III on Ce^{4+} (HCOO III)$_{ad}$	
1211 ~ 1216	δ(COH)	hydrogencarbonate (CO$_3$H)$_{ad}$	[49, 50]
1940 ~ 2000	ν(CO)	on-top adsorbed CO on cobalt (CO)$_{ad}$	[57, 58]
3016	ν(CH)	CH$_4$ gas phase (CH$_4$)$_g$	[59, 60]

Carbonate and hydrogencarbonate: **Figure S5** shows the region of 950 ~ 1120 cm^{-1} for the C-O stretching mode ν(CO) in carbonate and hydrogencarbonate. Detailed peak assignments are summarized in **Table 3** and **Table S4** (supporting information) [48-50, 52, 53, 61]. The adsorbed methoxy species on ceria can be excluded because its typical peak corresponding to ν(CH) at 2750 ~ 2810 cm^{-1} or the ν(CO) at 1100 ~ 1150 cm^{-1} was not observed [62, 63]. The 1200 ~ 1700 cm^{-1} region, where ν(CO) intensity is strong, was not used for analysis because overlapping of carbonate, hydrogencarbonate and formate peaks (**Table S4**) as well as water vapor features. Due to the different trends of peak evolution as the increasing reaction time, the peaks in the 950 ~ 1120 cm^{-1} region were assigned to four different carbonate species. Type I (CO$_3$ I)$_{ad}$: 1075 ~ 1085 cm^{-1} (polydentate carbonate on Ce^{3+}), type II (CO$_3$ II)$_{ad}$ or (CO$_3$H): 1041 ~ 1051 cm^{-1} (polydentate carbonate on Ce^{4+} and /or hydrogencarbonate), type III (CO$_3$ III)$_{ad}$: 1009 ~ 1015 cm^{-1} and type IV (CO$_3$ IV)$_{ad}$: 990 ~ 992 cm^{-1} (bidentate carbonates on different sites)[48-50, 52, 61]. According to the literature, the types III and IV carbonates are bidentate carbonates bound to different surface sites but their exact structures are unknown. Since the ν(CO) of hydrogencarbonate overlaps with that of polydentate carbonate, the existence of hydrogencarbonate was verified by the typical δ(COH) band [49, 50]. As shown in **Figure S6**, the peak at 1211 ~ 1216 cm^{-1} is assigned to the δ(COH) band of hydrogencarbonate. The concentrations of hydrogencarbonate in bare CeO$_2$ and 1wt% are much higher than those in 2wt% and 4wt% Co/CeO$_2$. Since hydrogen dissociation on bare ceria is known to be weak, the presence of the δ(COH) signal in

1wt%Co/CeO$_2$ indicates that it also has very weak diffusion of dissociated hydrogen[64]. The hydrogenation of hydrogencarbonate has been reported in literature [65], which could explain the weak δ(COH) band in 2wt% and 4wt%Co/CeO$_2$. For these reasons, hydrogencarbonate is only expected to be stable on the Ce^{4+} sites. **Figure 7** illustrates the evolution of carbonate and hydrogencarbonate after the introduction of carbon dioxide to yield a CO$_2$/H$_2$ mixture . It appears that the bidentate carbonate species (~990 cm^{-1} and ~1010 cm^{-1}) are not stable as they quickly reach their maximum intensity and start decreasing. The polydentate carbonate on Ce^{4+}/hydrogencarbonate (1041 ~ 1051 cm^{-1}) quickly levels off after 4 min while polydentate carbonate on Ce^{3+} (1075 ~1085 cm^{-1}) keeps increasing. With an increasing reaction time, the polydentate carbonate on Ce^{3+} (1078 ~ 1080 cm^{-1}) becomes dominant a species in 2wt% and 4wt%Co/CeO$_2$ while the polydentate carbonate on Ce^{4+} and/or hydrogencarbonate (1041 ~ 1041 cm^{-1}) are the major species on bared CeO$_2$ and 1wt%Co/CeO$_2$. This result suggests that 2wt% and 4wt%Co/CeO$_2$ have higher Ce^{3+} concentration than CeO$_2$ and 1wt%Co/CeO$_2$ under the reaction conditions.

Formate: It has been reported that several types of formates can be formed on ceria [48, 53, 66] but their ν$_{as}$(CO), ν$_s$(CO), and δ(OCH) peaks partially overlap with that of carbonates in the typical 1200-1700 cm^{-1} region as seen in **Table S4**. Moreover, the typical ν(CH) bands of different types of formate in the 2800 ~ 2900 cm^{-1} (**Figure S7**) region partially overlap with the combination band of carbonates [48]. The weak peaks observed in the region of 2700 ~ 2730 cm^{-1} (**Figure 8**) were reported and assigned to an overtone 2δ(OCH) band of formate [48, 54-56]. As these bands do not overlap with any other commonly observed species (**Table S4**), they were used to track the evolution of formate.

As for the formate 2δ(OCH) peaks, as shown in **Figure 8** and **S8**, there are major bands centered around 2710 cm^{-1} for the CeO$_2$ and Co/CeO$_2$ samples. In the cases of the 2wt% and 4wt% samples, the center of major peak stayed at 2710 cm^{-1} during the whole set of experiments while the position of the major band in the CeO$_2$ and 1wt%Co/CeO$_2$ gradually shifted to higher wavenumber during the IR measurements. The shifting of the 2710 cm^{-1} peak indicates that a new band is gradually growing at higher wavenumbers during the reaction. Meanwhile, a shoulder peak centered at around 2703 cm^{-1} was also seen in the 1wt%, 2wt% and 4wt%Co/CeO$_2$ systems even though the position of the band in the 4wt% seems to locate to a slightly lower wavenumber position.

In the literature, three types of formate (I, II, III) on partially reduced ceria has been reported, which could correspond to the three different 2δ(OCH) band positions. Formate III is generally believed to bond to Ce^{4+} while formate I and II bond on sites with oxygen vacancies[48, 53, 66]. Since the 2δ(OCH) band at wavenumbers higher than 2710 cm^{-1} was only observed in the CeO$_2$ and 1wt%Co/CeO$_2$, whose Ce^{4+} surface concentration is high, the band is assigned to formate on Ce^{4+} (formate III). And the 2703 cm^{-1} and 2710 cm^{-1} features could be assigned to formate I and II on Ce^{3+} sites, respectively. Formate II dominated on all four samples when CO$_2$ was introduced and formate I started to appear after about 10 mins. Different from 2wt% and 4wt% catalysts, formate III accounted for a considerable amount in formate at the end of 29 mins on the bare ceria and 1wt% systems. As formate should mostly form around the cobalt particles where there is more dissociated hydrogen[67], the different pattern of formate in the 1wt%Co/CeO$_2$ compared to the other two points to its different chemical environment even in the more active region. In addition, while formate I and II bands were observed in the experiments of both 2wt% and 4wt%Co/CeO$_2$ catalysts, the evolution of them were very different. After 7 min, the formate II, not leveling off like what was observed in the 2wt% sample, started decreasing in 4wt%Co/CeO$_2$. The decline of the formate II concentration in 4wt% may indicate a faster formate consumption than that of 2wt% Co/CeO$_2$.
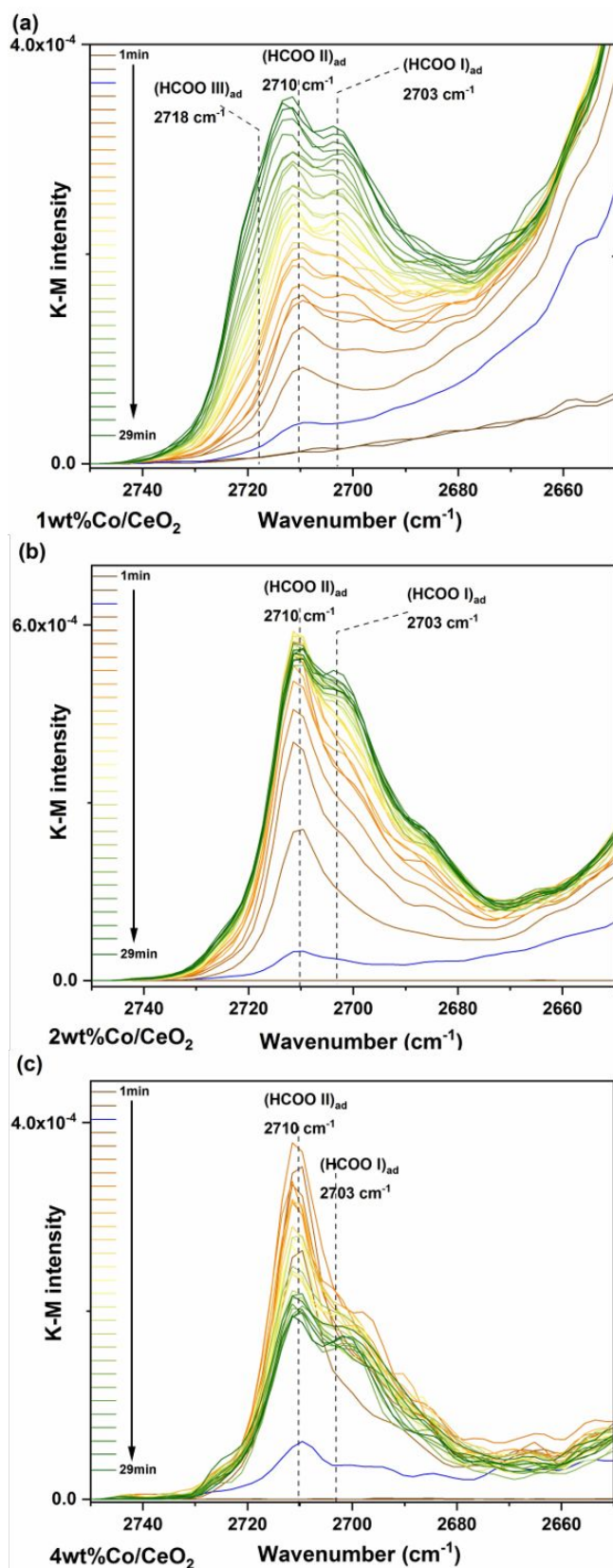
Figure 8. *In situ* DRIFTS data for (**a**) 1wt%Co/CeO$_2$, (**b**) 2wt% Co/CeO$_2$ and (**c**) 4wt% Co/CeO$_2$, collected at 250 °C, at 1 atm pressure, in the region of 2750-2650 cm^{-1} when gases were switched from 10 sccm H$_2$ into a {5 sccm H$_2$, 1 sccm CO$_2$, 1 sccm He} mixture at the 0 minute time.
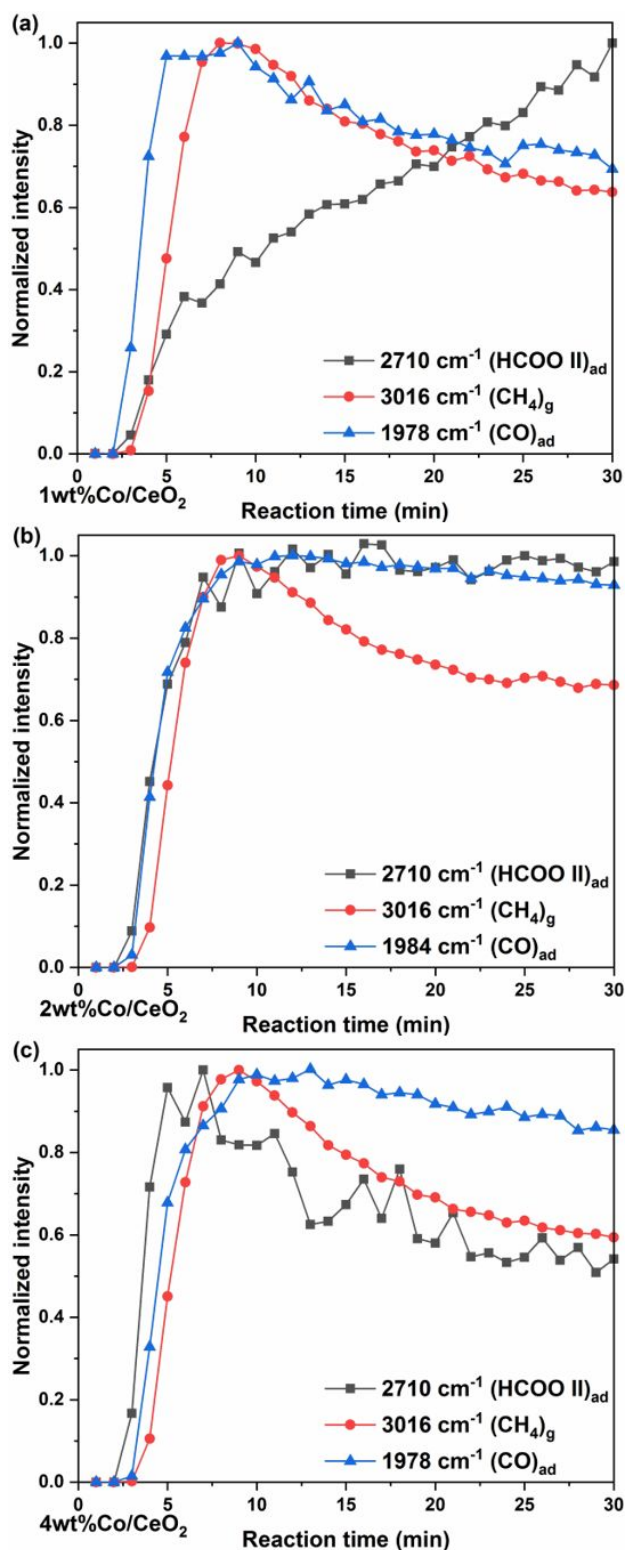
Figure 9. Evolution of adsorbed formate, adsorbed CO, and CH_4 gas determined from the height of the corresponding peaks in *in situ* DRIFTS data collected at 250 °C and 1atm. Gases were switched from 10 sccm H_2 into a {5 sccm H_2, 1 sccm CO_2, 1 sccm He} mixture at the 0 minute time. (**a**) 1wt%Co/CeO$_2$ (**b**) 2wt% Co/CeO$_2$ (**c**) 4wt% Co/CeO$_2$

Adsorbed CO: The detected signals from DRIFTS are mostly ascribed to adsorbed species on

14

ceria. On a cobalt surface, the only observable species is adsorbed CO, which was detected in all three samples in similar positions at $1978 \sim 1984 \ cm^{-1}$ (**Figure S9**) when the signals reached highest intensity. The peak was assigned to low coverage on-top (linear) carbonyls on metallic cobalt particles [57, 58]. No significant difference was observed between the three samples indicating there are metallic cobalt sites of similar structure on the surface of all samples (**Figure S9**).

     Evolution of species: To get information about the intermediates for CH_4 and CO production, the evolution of adsorbed CO, formate II and CH_4 gas were obtained from the *in situ* DRIFTS data. The height of the representative position for each species was normalized by their highest intensity and plotted as a function of time after CO_2 was introduced (**Figure 9**). It appears that the evolution of formate was very different among the three samples: Kept increasing in the whole 30 mins for 1wt%; reached a plateau at 9 mins for 2wt%; reached a maximum at 5-7 min and then declined for 4wt%. The different trends may result from rate differences between formate production and consumption. Even though evolution of formate is different among the three samples, their CH_4 gas phase evolution patterns are similar, suggesting that formate may not play a major role in CH_4 production. As for adsorbed CO, its evolution patterns were similar among the three samples: Reached a maximum at around 9 min and then slightly decreased. However, it is noticeable that the adsorbed CO on the 1wt% sample declines faster than on the other two.
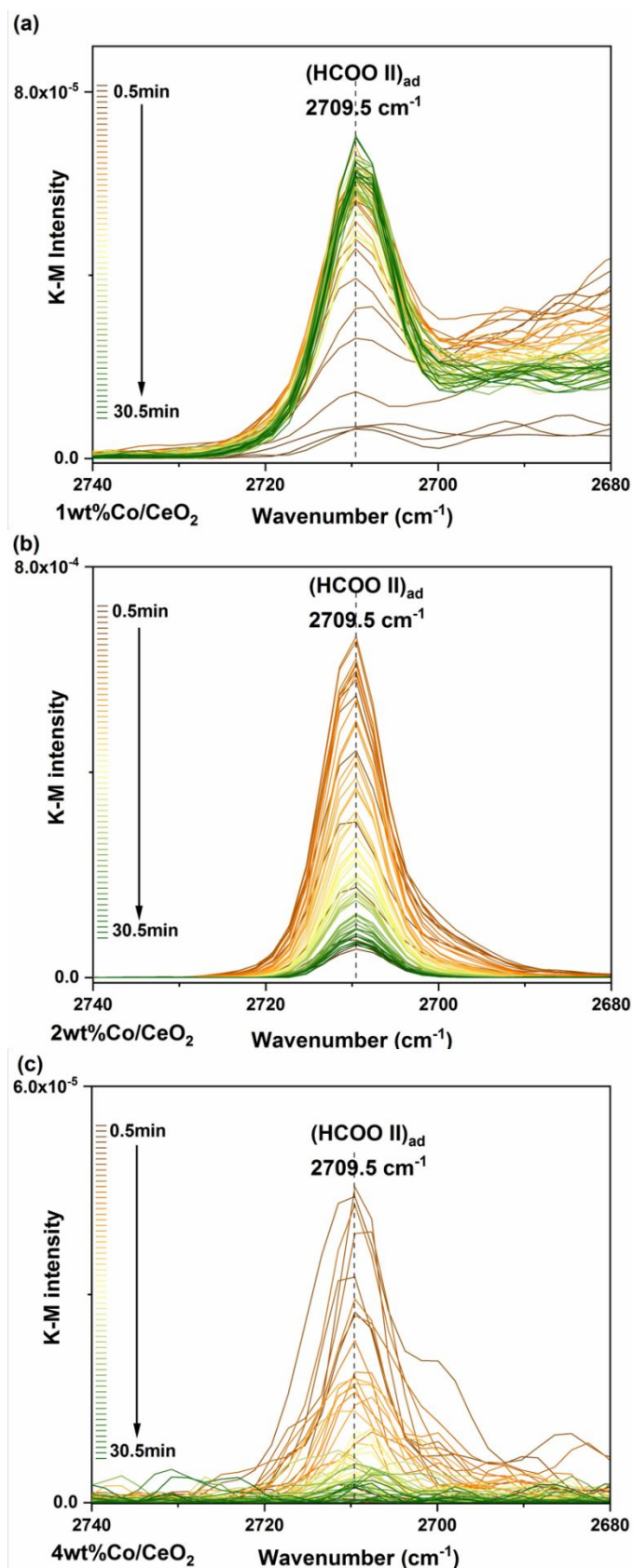
Figure 10. The intensity evolution in the region of 2690-2740 cm^{-1} collected in *in situ* DRIFTS during the closed system experiments for (**a**) 1wt%Co/CeO$_2$, (**b**) 2wt%Co/CeO$_2$ and (**c**) 4wt% Co/CeO$_2$ catalysts.

Experiments on a closed system: To further investigate the role of formate and CO in the reaction, experiments were also carried out in a closed system with a small amount (about 1v%) of CO_2 in H_2 to maximize CO_2 conversion.

Formate: The evolution of peak intensity for the formate $2\delta(OCH)$ feature is shown in **Figure 10**. In contrast to the continuous flow conditions, only a peak centered near 2709.5 cm^{-1} (formate II) appeared for all the three samples. This indicates that the formate in all samples adsorbs on a comparable Ce^{3+} site. However, the evolution of the formate intensity was dependent on the Co loading. The intensity of formate II in 1wt% Co remained constant after it reacheed a maximum. In the case of 2wt% and 4wt% Co, however, the formate II intensity decreased significantly with reaction time after it reached a maximum. Similar evolution was also observed in the $\nu(CH)$ band region (**Figure S10**).

Carbonate: As no similar $\delta(COH)$ band was observed (**Figure S11**) to the one detected in the flow system experiments, only the peaks at 950-1120 cm^{-1} can be attributed to carbonate species. The evolution of four major carbonate features is shown in **Figure 11 a, b and S14 a** and their original spectra are displayed in **Figure S12.** Different from the evolution in the flow system (**Figure 7**), all the carbonate species decreased with CO_2 after 5 min.

Adsorbed CO: Not like the flow system experiments, adsorbed CO was not detected in the 1wt% Co sample possibly due to its low concentration. As shown in **Figure S13**, the positions of the $\nu(CO)$ are at lower wavenumbers than those observed in the flow experiments due to even lower coverage. As shown in the **Figure 11 d and S11 b**, CO_2 gas phase and adsorbed CO reach a maximum at the same time, earlier than formate does.

Proposed reaction mechanism: as shown in **Figure 11** and **Figure S14**, both the CO and CO_2 reached maximum at same time. It could indicate that CO is directly formed from CO_2 and its consumption is very fast. As for formate, it is clear that it is a spectator in 1wt% Co (**Figure 11 c**) while it can be further hydrogenated in the 2wt% and 4wt% Co samples (**Figure 11 d** and **Figure S14 b**). According to literature[68], there are two major mechanisms for CO_2 methanation: (1) associative mechanism: the methanation process involves associative adsorption of CO_2 and the associated species are further hydrogenated to CH_4; (2). dissociative mechanism: CO_2 directly dissociates to adsorbed carbonyl followed by hydrogenation of carbonyl to CH_4. **Figure 12** illustrates the proposed mechanism for CO_2 hydrogenation on Co/CeO_2 catalysts: CO_2 can quickly be converted into CO without forming formate and the process of CO hydrogenation is the primary pathway for CH_4 production (dissociative mechanism). When there are sufficient hydrogen atoms migrating from cobalt particles to adjacent ceria regions, the formate also can be further hydrogenated (associative mechanism). However, the formate pathway is not the major channel for either CO or CH_4 production. In the process of methanation, if carbonyl production is faster than its consumption, part of it will desorb into CO gas phase which is seen in the conditions of our catalytic activity measurements.
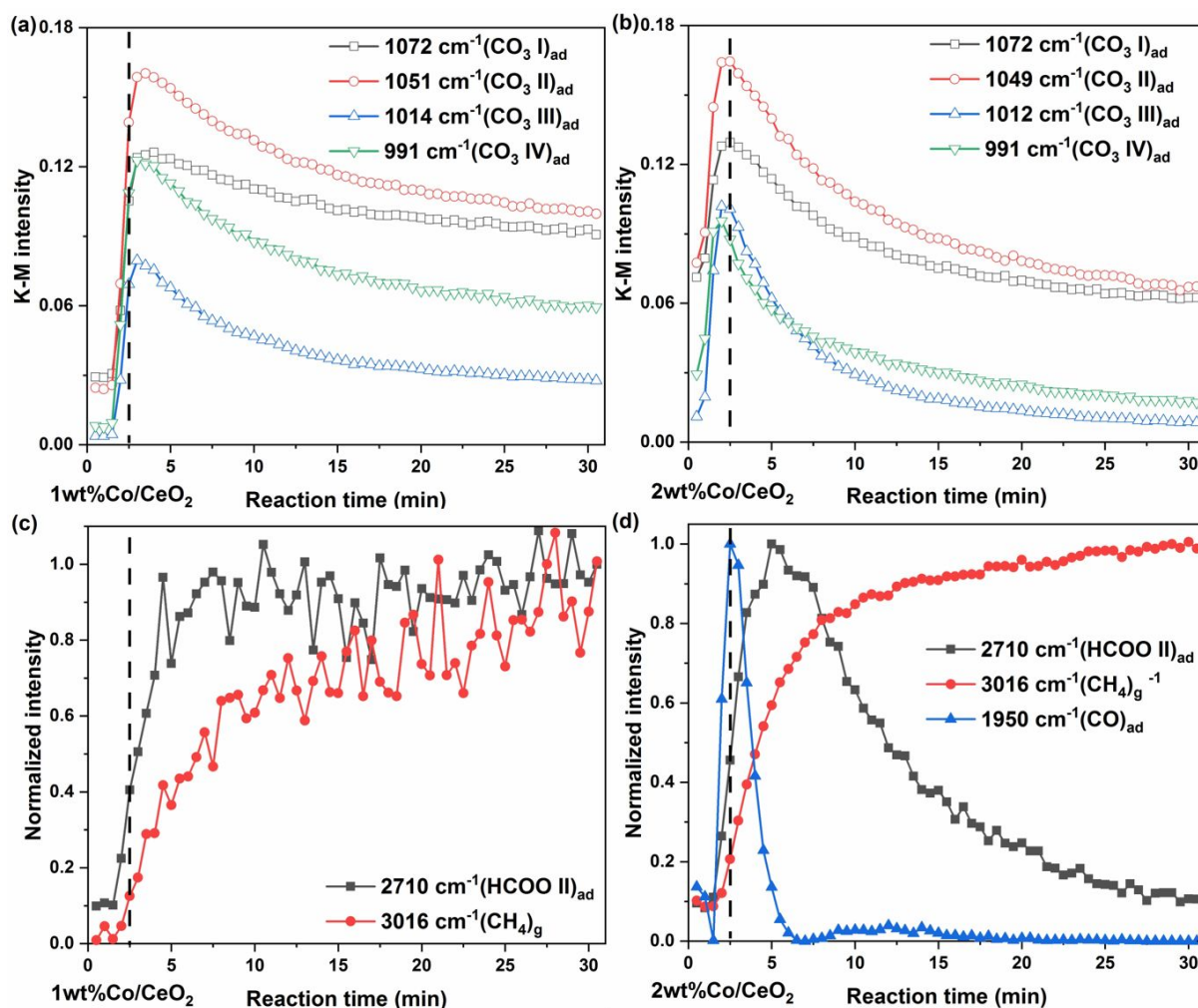
Figure 11. Evolution of formate, adsorbed CO, CH$_4$ gas phase and carbonate species, with corresponding normalized peak intensity, derived from *in situ* DRIFTS experiments on a closed system at 250 °C, 1 atm pressure. Approximate 1v%CO$_2$ in H$_2$ was introduced into the cell before valves were switched off. Evolution of carbonate species of (**a**)1wt%Co/CeO$_2$ (**b**) 2wt%Co/CeO$_2$. Evolution of formate, adsorbed CO, CH$_4$ gas phase of (**c**) 1wt%Co/CeO$_2$ (**d**) 2wt%Co/CeO$_2$. The highest CO$_2$ concentration was observed at 2.5 min (marked with dash).
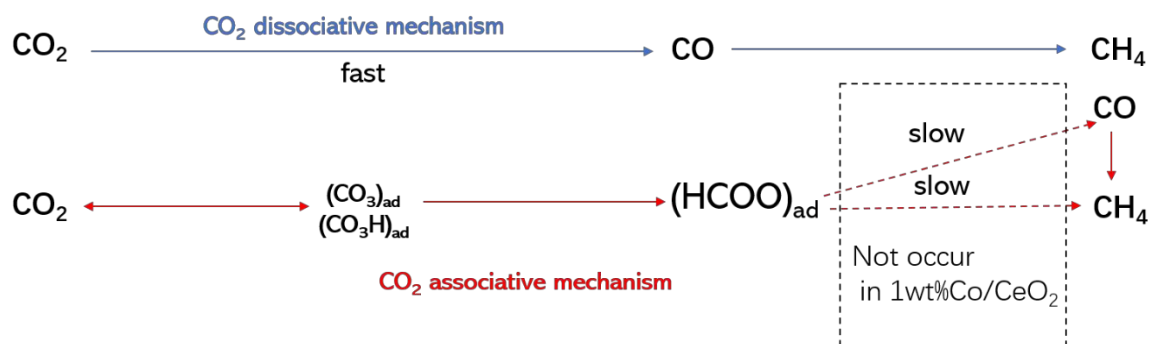
Figure 12. Scheme of the proposed reaction mechanism for CO$_2$ hydrogenation on Co-ceria catalysts. The dissociative mechanism is marked in blue arrows while red arrows indicate the associative mechanism pathway.

Conclusions

1. In this study, three Co/CeO$_2$ catalysts were tested for their activity for CO$_2$ hydrogenation. With the same weight of cobalt, the activity showed the trend: 4wt% $\approx$ 2wt% > 1wt%.

2. For pristine samples, a Co$_3$O$_4$ diffraction pattern was observed in XRD in pristine 2wt% and 4wt% Co while no cobalt-based phase was observed in the 1wt% Co sample. After reduction, weak CoO and a fcc Co patterns were observed for the 4wt% Co sample, while no diffraction pattern was seen for 1wt% and 2wt% Co/CeO$_2$. The results indicate that the 4wt% Co system had the largest cobalt particle size among the series.

3. XANES results for pristine and reduced samples showed that the CoO concentration followed the trend: 1wt% > 2wt% > 4wt%. As CoO is expected to be stable near the cobalt/ceria interface under oxidized and reduced conditions, it is likely that, in the 1wt% Co/CeO$_2$ sample, the relative amount of cobalt atoms near the interface was larger than that of in the other samples. 1wt% Co/CeO$_2$ displayed the strongest effects of metal-support interactions with a chemistry that was different from that of the two other cobalt-ceria samples and cobalt supported on non-interacting oxides.

4. The analysis on the EXAFS data shows that the cobalt particle size in the reduced 4wt% Co/CeO$_2$ is around 2.5 nm with lower bound and upper bound limits at 2.0 and 3.3 nm. The Co-O bonding in the reduced 1wt% and 2wt% Co/CeO$_2$ have a shorter bond length than that of standard CoO by about 0.16 Å. The strong bonding explains the stability of part of CoO during reduction for those lower loading catalysts.

5. *In situ* NAP-XPS data of the reduced samples showed that the Ce^{3+} concentration followed the sequence 4wt% $\approx$ 2w% > 1wt% and the cobalt in the 4wt% sample was primarily metallic under reaction conditions.

6. *In situ* DRIFTS results showed that formate was only a spectator in the 1wt% Co sample while formate in 2wt% and 4wt% Co could be further hydrogenated. In any case, it appears that direct CO hydrogenation into CH$_4$ was the primary pathway for methane production

7. The direct cause for the lower CO$_2$ hydrogenation efficiency of 1wt%Co/CeO$_2$ was its weaker ability to activate hydrogen. Fundamentally, it could result from exposing positively charged cobalt atoms directly interacting with CeO$_2$.

Reference

1.	X. Su, J. Xu, B. Liang, H. Duan, B. Hou and Y. Huang, *Journal of Energy Chemistry*, 2016, **25**, 553-565.

2.	S. G. Jadhav, P. D. Vaidya, B. M. Bhanage and J. B. Joshi, *Chemical Engineering Research and Design*, 2014, **92**, 2557-2567.

3.	R.-P. Ye, J. Ding, W. Gong, M. D. Argyle, Q. Zhong, Y. Wang, C. K. Russell, Z. Xu, A. G. Russell, Q. Li, M. Fan and Y.-G. Yao, *Nature Communications*, 2019, **10**, 5698.

4.	C. Yang, R. Mu, G. Wang, J. Song, H. Tian, Z.-J. Zhao and J. Gong, *Chemical Science*, 2019, **10**, 3161-3167.

5.	Z. Li, J. Wang, Y. Qu, H. Liu, C. Tang, S. Miao, Z. Feng, H. An and C. Li, *ACS Catalysis*, 2017, **7**, 8544-8548.

6.	J. Wei, Q. Ge, R. Yao, Z. Wen, C. Fang, L. Guo, H. Xu and J. Sun, *Nature Communications*, 2017, **8**, 15174.

7.	S. Kattel, P. Liu and J. G. Chen, *Journal of the American Chemical Society*, 2017, **139**, 9739-9754.

8.	J. A. Rodriguez, P. Liu, D. J. Stacchiola, S. D. Senanayake, M. G. White and J. G. Chen, *ACS Catalysis*, 2015, **5**, 6696-6706.

9.	S. Kattel, B. Yan, Y. Yang, J. G. Chen and P. Liu, *Journal of the American Chemical Society*, 2016, **138**, 12440-12450.

10.	L. Kristinsdóttir and E. Skúlason, *Surface Science*, 2012, **606**, 1400-1404.

11.	G. D. Weatherbee and C. H. Bartholomew, *Journal of Catalysis*, 1982, **77**, 460-472.

12.	E. Iglesia, *Applied Catalysis A: General*, 1997, **161**, 59-78.

13.	C. A. Chanenchuk, I. C. Yates and C. N. Satterfield, *Energy & Fuels*, 1991, **5**, 847-855.

14. C. G. Visconti, M. Martinelli, L. Falbo, L. Fratalocchi and L. Lietti, *Catalysis Today*, 2016, **277**, 161-170.

15. J. Lahtinen, T. Anraku and G. A. Somorjai, *Catalysis Letters*, 1994, **25**, 241-255.

16. V. A. de la Peña O'Shea, S. González, F. Illas and J. L. G. Fierro, *Chemical Physics Letters*, 2008, **454**, 262-268.

17. J. Díez-Ramírez, P. Sánchez, V. Kyriakou, S. Zafeiratos, G. E. Marnellos, M. Konsolakis and F. Dorado, *Journal of CO2 Utilization*, 2017, **21**, 562-571.

18. T. Staudt, Y. Lykhach, N. Tsud, T. Skála, K. C. Prince, V. Matolín and J. Libuda, *The Journal of Physical Chemistry C*, 2011, **115**, 8716-8724.

19. J. B. Park, J. Graciani, J. Evans, D. Stacchiola, S. D. Senanayake, L. Barrio, P. Liu, J. F. Sanz, J. Hrbek and J. A. Rodriguez, *Journal of the American Chemical Society*, 2010, **132**, 356-363.

20. S. Li, Y. Xu, Y. Chen, W. Li, L. Lin, M. Li, Y. Deng, X. Wang, B. Ge, C. Yang, S. Yao, J. Xie, Y. Li, X. Liu and D. Ma, *Angewandte Chemie International Edition*, 2017, **56**, 10761-10765.

21. Z. Liu, F. Zhang, N. Rui, X. Li, L. Lin, L. E. Betancourt, D. Su, W. Xu, J. Cen, K. Attenkofer, H. Idriss, J. A. Rodriguez and S. D. Senanayake, *ACS Catalysis*, 2019, **9**, 3349-3359.

22. S. W. Ho, M. Houalla and D. M. Hercules, *The Journal of Physical Chemistry*, 1990, **94**, 6396-6399.

23. S.-W. Ho, J. M. Cruz, M. Houalla and D. M. Hercules, *Journal of Catalysis*, 1992, **135**, 173-185.

24. S. Zhang, Y. Li, J. Huang, J. Lee, D. H. Kim, A. I. Frenkel and T. Kim, *The Journal of Physical Chemistry C*, 2019, **123**, 7166-7177.

25. B. H. Toby and R. B. Von Dreele, *Journal of Applied Crystallography*, 2013, **46**, 544-549.

26. H. Rietveld, *Journal of Applied Crystallography*, 1969, **2**, 65-71.

27.   B. Ravel and M. Newville, *Journal of Synchrotron Radiation*, 2005, **12**, 537-541.

28.   M. Newville, *Journal of Synchrotron Radiation*, 2001, **8**, 322-324.

29.   T. Skála, F. Šutara, K. C. Prince and V. Matolín, *Journal of Electron Spectroscopy and Related Phenomena*, 2009, **169**, 20-25.

30.   M. L. Trudeau, A. Tschöpe and J. Y. Ying, *Surface and Interface Analysis*, 1995, **23**, 219-226.

31.   F. ç. Larachi, J. Pierre, A. Adnot and A. Bernis, *Applied Surface Science*, 2002, **195**, 236-250.

32.   S. Kato, M. Ammann, T. Huthwelker, C. Paun, M. Lampimäki, M.-T. Lee, M. Rothensteiner and J. A. van Bokhoven, *Physical Chemistry Chemical Physics*, 2015, **17**, 5078-5083.

33.   K. O'Connell and J. R. Regalbuto, *Catalysis Letters*, 2015, **145**, 777-783.

34.   V. Bartůněk, Š. Huber, D. Sedmidubský, Z. Sofer, P. Šimek and O. Jankovský, *Ceramics International*, 2014, **40**, 12591-12595.

35.   Y. Ji, Z. Zhao, A. Duan, G. Jiang and J. Liu, *The Journal of Physical Chemistry C*, 2009, **113**, 7186-7199.

36.   A. Chen, X. Yu, Y. Zhou, S. Miao, Y. Li, S. Kuld, J. Sehested, J. Liu, T. Aoki, S. Hong, M. F. Camellone, S. Fabris, J. Ning, C. Jin, C. Yang, A. Nefedov, C. Wöll, Y. Wang and W. Shen, *Nature Catalysis*, 2019, **2**, 334-341.

37.   A. M. Beale and B. M. Weckhuysen, *Physical Chemistry Chemical Physics*, 2010, **12**, 5562-5574.

38.   P. Eisenberger and B. M. Kincaid, *Science*, 1978, **200**, 1441.

39.   P. H. Citrin, P. Eisenberger and B. M. Kincaid, *Physical Review Letters*, 1976, **36**, 1346-1349.

40.   G. Melaet, A. E. Lindeman and G. A. Somorjai, *Topics in Catalysis*, 2014, **57**, 500-507.

41.   V. Iablokov, S. K. Beaumont, S. Alayoglu, V. V. Pushkarev, C. Specht, J. Gao, A. P. Alivisatos,

N. Kruse and G. A. Somorjai, *Nano Letters*, 2012, **12**, 3091-3096.

42.   J. C. Matsubu, V. N. Yang and P. Christopher, *Journal of the American Chemical Society*, 2015, **137**, 3076-3084.

43.   E. Bêche, P. Charvin, D. Perarnau, S. Abanades and G. Flamant, *Surface and Interface Analysis*, 2008, **40**, 264-267.

44.   D. Tian, K. Li, Y. Wei, X. Zhu, C. Zeng, X. Cheng, Y. Zheng and H. Wang, *Physical Chemistry Chemical Physics*, 2018, **20**, 11912-11929.

45.   W.-J. Wang and Y.-W. Chen, *Applied Catalysis*, 1991, **77**, 223-233.

46.   H. Sohn, G. Celik, S. Gunduz, D. Dogu, S. Zhang, J. Shan, F. F. Tao and U. S. Ozkan, *Catalysis Letters*, 2017, **147**, 2863-2876.

47.   W. C. Conner and J. L. Falconer, *Chemical Reviews*, 1995, **95**, 759-788.

48.   G. N. Vayssilov, M. Mihaylov, P. S. Petkov, K. I. Hadjiivanov and K. M. Neyman, *The Journal of Physical Chemistry C*, 2011, **115**, 23435-23454.

49.   C. Binet, M. Daturi and J.-C. Lavalley, *Catalysis Today*, 1999, **50**, 207-225.

50.   O. Pozdnyakova, D. Teschner, A. Wootsch, J. Kröhnert, B. Steinhauer, H. Sauer, L. Toth, F. C. Jentoft, A. Knop-Gericke, Z. Paál and R. Schlögl, *Journal of Catalysis*, 2006, **237**, 17-28.

51.   C. Li, Y. Sakata, T. Arai, K. Domen, K.-i. Maruya and T. Onishi, *Journal of the Chemical Society, Faraday Transactions 1: Physical Chemistry in Condensed Phases*, 1989, **85**, 929-943.

52.   C. Binet, A. Badri, M. Boutonnet-Kizling and J.-C. Lavalley, *Journal of the Chemical Society, Faraday Transactions*, 1994, **90**, 1023-1028.

53.   P. G. Lustemberg, M. V. Bosco, A. Bonivardi, H. F. Busnengo and M. V. Ganduglia-Pirovano, *The Journal of Physical Chemistry C*, 2015, **119**, 21452-21464.

54.   T. L. Charlton and K. B. Harvey, *Canadian Journal of Chemistry*, 1966, **44**, 2717-2727.

55.   K. B. Harvey, B. A. Morrow and H. F. Shurvell, *Canadian Journal of Chemistry*, 1963, **41**, 1181-1187.

56.   M. A. Moreno, O. Gálvez, B. Maté, V. J. Herrero and R. Escribano, *The Journal of Physical Chemistry A*, 2011, **115**, 70-75.

57.   G. Busca, R. Guidetti and V. Lorenzelli, *Journal of the Chemical Society, Faraday Transactions*, 1990, **86**, 989-994.

58.   K. M. Rao, G. Spoto and A. Zecchina, *Journal of Catalysis*, 1988, **113**, 466-474.

59.   R. W. Stevens and S. S. C. Chuang, *The Journal of Physical Chemistry B*, 2004, **108**, 696-703.

60.   K. Otsuka, Y. Wang, E. Sunada and I. Yamanaka, *Journal of Catalysis*, 1998, **175**, 152-160.

61.   C. Li, Y. Sakata, T. Arai, K. Domen, K.-i. Maruya and T. Onishi, *Journal of the Chemical Society, Faraday Transactions 1: Physical Chemistry in Condensed Phases*, 1989, **85**, 1451-1461.

62.   A. Badri, C. Binet and J.-C. Lavalley, *Journal of the Chemical Society, Faraday Transactions*, 1997, **93**, 1159-1168.

63.   C. Binet and M. Daturi, *Catalysis Today*, 2001, **70**, 155-167.

64.   J. El Fallah, S. Boujana, H. Dexpert, A. Kiennemann, J. Majerus, O. Touret, F. Villain and F. Le Normand, *The Journal of Physical Chemistry*, 1994, **98**, 5522-5533.

65.   X. Wang, H. Shi, J. H. Kwak and J. Szanyi, *ACS Catalysis*, 2015, **5**, 6337-6349.

66.   T. Tabakova, F. Boccuzzi, M. Manzoli and D. Andreeva, *Applied Catalysis A: General*, 2003, **252**, 385-397.

67.   V. Sharma, P. A. Crozier, R. Sharma and J. B. Adams, *Catalysis Today*, 2012, **180**, 2-8.

68.   B. Miao, S. S. K. Ma, X. Wang, H. Su and S. H. Chan, *Catalysis Science & Technology*, 2016,

6, 4048-4058.

TOC
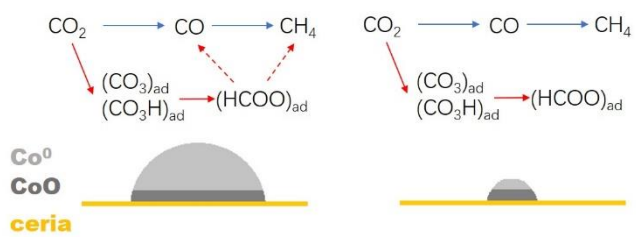
Metal-oxide interactions affect the catalytic properties of Co/CeO_2 and can be used to control activity and selectivity